A Low-Cost IoT-Based Irradiance Estimator for Photovoltaic Modules

Pedro Henrique da Costa Eustáchio[1], Gustavo Medeiros de Souza Azevedo[1], Eduardo José Barbosa[1], Marcelo Cabral Cavalcanti[1], Fabrício Bradaschia[1], Rafael Cavalcanti Neto[1], Tiago Alves Fernandes[1] and José Filho da Costa Castro[1]

[1] UFPE – Universidade Federal de Pernambuco, Recife (Brazil)

Abstract

This paper presents the development of a low-cost and low-complexity irradiance estimator for photovoltaic (PV) systems, combining a Lookup Table (LUT)-based approach with an Internet of Things (IoT) communication framework. The proposed system integrates hardware improvements, including a high-resolution external ADC and an ESP32 microcontroller, to overcome previous limitations in measurement accuracy. A key innovation is the decentralization of data processing, executing the estimation algorithm via a Python process on a remote computer, enabling the use of larger LUTs and facilitating system maintenance. Simulation results demonstrated high accuracy with a Mean Absolute Percentage Error (MAPE) of 1.56% using an optimized LUT, while experimental validation yielded a MAPE of 2.42%. The system successfully implements MQTT protocol for real-time data transmission, establishing a foundation for remote PV monitoring. Analysis under partial shading confirmed the estimator's capability to identify predominant irradiance levels, while revealing limitations in transition regions due to the uniform-irradiance assumption of the underlying global nonlinear model (GNLM).

Keywords: Irradiance Estimation, Photovoltaic Systems, IoT, GNLM, Lookup Table.

1. Introduction

Monitoring photovoltaic (PV) modules is essential to ensure high performance and maximize energy generation. In this regard, irradiance measurement directly impacts system efficiency, enabling maximum power point tracking and the detection of critical operating conditions (Madureira et al., 2020).

While conventional Maximum Power Point Tracking (MPPT) algorithms predominantly rely on the PV array's own electrical signals, advanced Global MPPT (GMPPT) techniques can achieve higher speed and accuracy by incorporating the effects of irradiance and temperature to estimate the Maximum Power Point (MPP) (Barbosa et al., 2024a). Furthermore, the irradiance is also important for system diagnostics. A study on fault detections used machine learning techniques to evaluate how abrupt variations in module power could be caused by failures or natural irradiance variations, demonstrating that the power delivered by a PV system is strongly dependent on irradiance (Hajji et al., 2023). Based on weather conditions, Yildiz and Gol (2019) developed a neural network-based method to automatically identify faults in inverters and PV modules. Similarly, Lazzaretti et al. (2020) proposed a linear recursion model for system fault detection. Therefore, accurate irradiance assessment significantly enhances MPPT and enables the detection of various critical operating conditions.

However, obtaining this data through dedicated sensors such as pyranometers is often impractical due to their high cost and need for periodic calibration. Additionally, from a spatial perspective, these devices provide a measurement from a single point in the PV field. When one pyranometer is deployed for an entire array, its data inherently assumes uniform irradiance, a condition that is frequently violated in large installations or under partial shading. As a result, various irradiance estimation techniques have been investigated as cost-effective and efficient alternatives (Madureira et al., 2020; Barbosa et al., 2024b).

In the search for practical irradiance estimation solutions, methods ranging from traditional statistical

10.18086/swc.2025.04.30 Available at http://proceedings.ises.org

techniques to advanced neural networks have been explored. For instance, Carrasco et al. (2014) proposed an estimator that stands out for its low-cost hardware, implemented on an Arduino Uno. However, its simplistic approach, assuming constant irradiance, compromised accuracy. Chouay and Ouassaid (2024) employed a neural network using Short-Circuit Current (Isc) and Open-Circuit Voltage (Voc) as inputs, achieving a Mean Absolute Percentage Error (MAPE) of 1.19%, but at the expense of high computational cost and compromised energy generation. Alarcon-Maza et al. (2023) applied linear regression between Isc and irradiance, obtaining a MAPE of 6.97% and integrating Internet of Things (IoT) capabilities, which represents a relevant contribution to PV applications.

In this context, the method proposed by Barbosa et al. (2024b) stands out as a low-cost and low-complexity solution, based on a Lookup Table (LUT) and measurements of current (I), voltage (V), and temperature (T). By not relying on Isc or Voc, it preserves energy generation during operation. Implemented on an ESP8266 microcontroller, it achieved a MAPE of 3.53%, balancing accuracy, simplicity, and feasibility for PV systems. While this approach addresses several gaps from previous works, a detailed analysis reveals some important drawbacks:

- **Multiplexer**: An analog multiplexer was used due to the ESP8266's limitation of having only one analog-to-digital converter (ADC). This component reduces the sampling rate, introduces phase shifts between signals, and increases power consumption, hindering continuous monitoring applications.
- **Nonlinear ADC**: The 10-bit analog input of the ESP8266 exhibits nonlinearity, especially near the extremes of its range, which compromises measurement accuracy and often requires software correction.
- **LUT size**: The estimation accuracy depends on the LUT resolution. In the original work, although larger tables reduced the estimation error, the ESP8266's limited memory constrained the table size.
- **IoT communication**: Although Barbosa et al. (2024) highlighted the potential of the ESP8266's built-in Wi-Fi module, their work does not present a functional implementation of wireless communication for data transmission. This feature is essential for the integration of the estimator into remote supervisory systems.

In this work, a more robust irradiance estimator is proposed, building upon the approach of Barbosa et al. (2024b) and incorporating hardware enhancements and IoT communication, as detailed in the following section.

2. Irradiance Estimator

The estimation method adopted in this work is based on the principle that a PV module, when subjected to specific irradiance (G) and temperature (T) conditions, exhibits a unique current–voltage (I–V) characteristic curve. Therefore, from instantaneous measurements of I, V and T, it is possible to estimate the irradiance incident on the module at a given time.

The relationship between the environmental parameters (G, T) and the corresponding electrical characteristics of the module (I, V) can be described using a Global Nonlinear Model (GNLM). These models are capable of generating characteristic curves that accurately represent the actual behavior of the module under different G and T conditions (Zhang et al., 2022; Lu et al., 2022). In the estimator proposed by Barbosa et al. (2024b), the global model applied was developed by Silva et al. (2017).

This GNLM is based on the Single Diode Model (SDM) and enhances its formulation by considering the physical behavior of the PV module. To achieve this, the five original parameters of the SDM are adjusted through a parameterization process using experimental curves, increasing the total number of model parameters to eight. Although this approach increases the model's complexity, it allows accurate determination of the module's behavior under different environmental conditions.

However, the model consists of a set of nonlinear and transcendental equations, which results in a high computational cost. To overcome this limitation, the curves generated by the model can be used to correlate each irradiance value with several (I, V, T) triplets, forming a three-dimensional table that can be easily accessed through a LUT approach, eliminating the need to solve the full set of equations at each iteration.

Based on this strategy, the irradiance estimation algorithm presented here consists of two main steps: measuring the instantaneous values of current (I), voltage (V), and temperature (T); and estimating the irradiance through a LUT procedure.

The estimation step consists of finding, within the LUT, the two closest values surrounding the measured I, V, and T data, resulting in eight triplets (2^3) that correspond to eight G values interpreted as the vertices of a cube, as illustrated in Figure 1. To improve the accuracy of the estimation, a trilinear interpolation is then applied to these eight G values. The result of this interpolation corresponds to the central point of the cube (Figure 6), which represents the approximation of the function value at a midpoint.

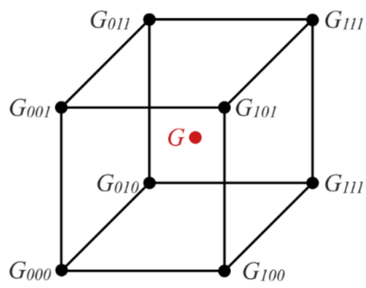

Figure 1: Trilinear Interpolation for Irradiance Estimation.

As a preliminary step to the estimation process, it is necessary to construct the LUT for the evaluated PV module. This is a one-time procedure and does not affect the computational complexity of the algorithm. Consequently, the algorithm requires only a reduced number of instructions to be executed by the microcontroller, ensuring a high execution rate in the order of microseconds.

Once the LUT is generated and the estimation algorithm is defined, a dedicated hardware architecture is designed to consolidate the previously discussed enhancements into a functional embedded system, representing an enhanced version of the work by Barbosa et al. (2024b). In this sense, the proposed system requires a minimum hardware setup composed of: three sensors (I, V, and T), signal conditioning circuits, an external ADC, a microcontroller, and a MQTT broker. The sensors perform simultaneous measurements, the ADC ensures high-precision signal digitization, and the microcontroller processes and transmits the data using the MQTT protocol. Finally, the MQTT broker enables the implementation of IoT communication.

From a software perspective, the system relies on two distinct scripts. The first one runs on the microcontroller and is responsible for data acquisition and transmission via the MQTT protocol. The second script, implemented in Python, executes the irradiance estimation algorithm. It receives the data published by the microcontroller through the MQTT broker, processes the information, and computes the irradiance estimate. This script, which hosts the LUT, runs on the same device that hosts the MQTT broker.

This separation in data processing between the microcontroller and the Python script enables the use of a larger LUT than what could be accommodated within the microcontroller's memory, addressing a limitation identified in Barbosa et al. (2024b). Figure 2 shows the schematic of the proposed irradiance estimation system.

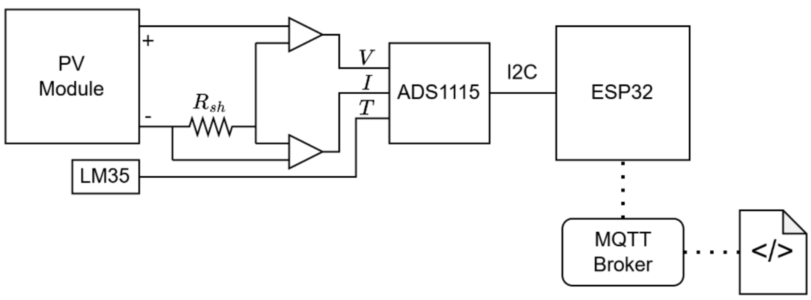

Figure 2: Schematic of proposed irradiance estimator with IoT communication.

The interaction between these hardware and software components follows a defined sequence to execute the estimation task. The operation of the irradiance estimator begins with an initialization phase, during which the MQTT broker is activated and connections are established with the ESP32 microcontroller and the Python script. The system then enters the estimation cycle, which includes the following steps: acquisition of I, V, and T signals; analog signal conditioning; digital conversion via the external ADC; and initial processing on the ESP32, converting the digital data into physical quantities. The ESP32 then sends the data to the MQTT broker, which forwards it to the Python script. The script runs the estimation algorithm and returns the estimated irradiance value. This cycle is continuously repeated to provide periodic updates of the irradiance estimation. Figure 3 shows the simplified flowchart of the described irradiance estimator.

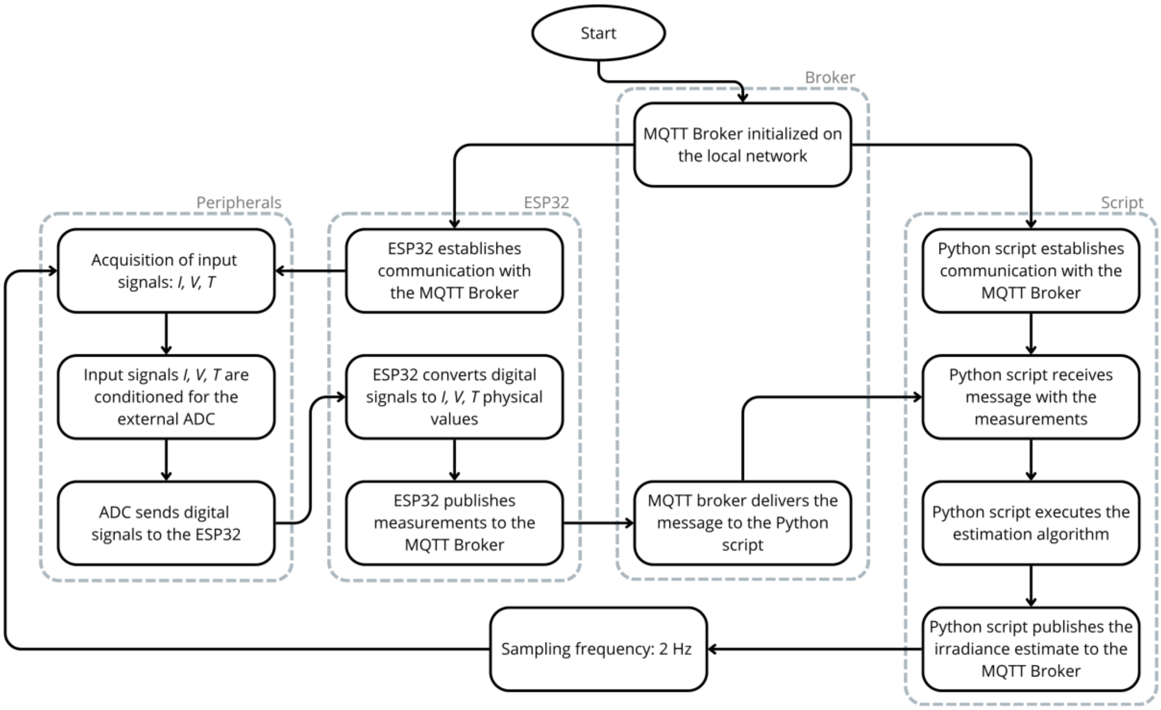

Figure 3: Simplified flowchart of the irradiance estimator with MQTT communication.

Following the system design, a physical prototype was assembled using readily available printed circuit boards (PCBs) that had been previously fabricated for other projects. The necessary interconnections between these boards were established to form a complete functional system. One PCB was primarily dedicated to the PV module connections and the analog signal conditioning circuit, while the other housed the external ADC and the microcontroller. Figure 4 shows the top and bottom views of the assembled irradiance estimator prototype.

3. Results and Discussion

This section presents and discusses the results obtained for the proposed irradiance estimation system, encompassing both numerical simulation and experimental validation. The analysis begins with the evaluation of the GNLM accuracy and the determination of the optimal LUT dimensions based on simulation data. Subsequently, the experimental results are presented, validating the system's performance and communication architecture under laboratory-controlled conditions, including uniform and partial shading conditions.

3.1. Simulation Results

The GNLM was initially applied to the Canadian Solar CS6W-555MS PV module, aiming to generate the LUT used in the irradiance estimation technique. The model was built following the approach described by Barbosa et al. (2024b), which employed experimental I-V curves collected under various environmental conditions for the parameterization process. These curves were acquired using the PVA-1000S curve tracer by Solmetric.

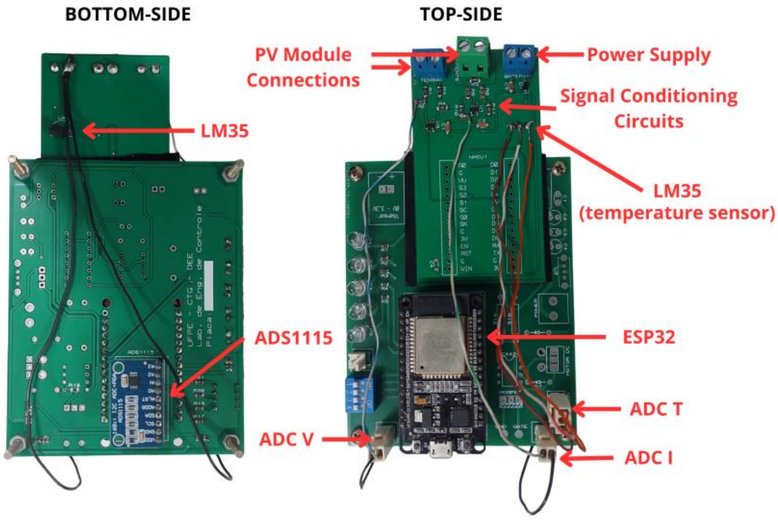

Figure 4: Assembled prototype of the proposed irradiance estimator.

To evaluate the accuracy of the developed model, the following performance metrics were calculated: the Mean Absolute Percentage Error (MAPE) and the normalized Root Mean Square Deviation (nRMSD). Their mathematical expressions are presented below:

$$MAPE = \frac{100\%}{N}\sum_{i=1}^{N}\left|\frac{y_i-\hat{y}_i}{y_i}\right|; \qquad \text{(eq. 1)}$$

$$nRMSD = \frac{100\%}{y_{max}-y_{min}}\sqrt{\frac{1}{N}\sum_{i=1}^{N}(y_i-\hat{y}_i)^2} \qquad \text{(eq. 2)}$$

Where y_i represents the experimentally measured values, $\hat{y}_i$ the values calculated by the model, N the total number of evaluated points, and y_{max} and y_{min} the maximum and minimum values of the analyzed variable.

Thus, to evaluate the accuracy of the GNLM, the experimental curves from the parameterization dataset were compared to their simulated counterparts generated by the model. Table 1 presents the environmental conditions under which the model was evaluated, along with the corresponding error metrics. Furthermore, the table includes the average value for each metric. These average values reflect the overall accuracy of the GNLM across the environmental conditions used during the parameterization step.

Table 1: Parameterization dataset and GNLM error metrics.

G (W/m2)	T (°C)	MAPE (%)	nRMSD (%)
1017	57	0.86	1.4
952	60	0.67	0.9
707	38	1.8	2.0
578	41	0.34	0.47
443	39	2.9	3.5
257	47	2.2	3.9
Mean (%)		**1.47**	**2.02**

From the generated model, it is possible to estimate the irradiance based on the operational (I, V, T) values. Accordingly, a LUT was to associate each combination of (I, V, T) with the corresponding irradiance value provided by the GNLM. Following this principle, different table dimensions were evaluated, (32×32×32), (64×64×64), (128×64×64), and (256×64×64), corresponding to (I×V×T) to determine the optimal size for estimation.

In the last two configurations, the increase in resolution was applied exclusively to the current axis. This decision was based on the current's nonlinear behavior in the I-V curve, which, as reported by Barbosa et al.

(2024b), leads to more pronounced percentage errors after the maximum power point voltage (V_{mpp}). Therefore, increasing the resolution along the current axis was adopted as a strategy to mitigate these errors.

Therefore, the four table configurations were evaluated using a set of ten distinct environmental conditions, considering all scenarios at the MPP. Table 2 presents the evaluated table dimensions and the corresponding estimation results under different irradiance and temperature conditions. Additionally, the table displays the estimation MAPE for each table dimension.

Table 2: Estimated irradiance at the MPP under different environmental conditions.

Measurement			32x32x32		64x64x64		128x64x64		256x64x64	
V_{mpp} (V)	G (W/m²)	T (ºC)	Gest (W/m²)	E (%)	Gest (W/m²)	E (%)	Gest (W/m²)	E (%)	Gest (W/m²)	E (%)
37.17	280	49	229.72	17.96	268.33	4.17	281.36	0.49	287.03	2.51
37.83	349	48	289.70	16.99	327.90	6.04	344.17	1.38	346.13	0.82
38.19	479	46	413.94	13.58	449.33	6.19	463.61	3.21	467.01	2.50
37.19	538	47	476.27	11.47	514.60	4.35	520.55	3.24	531.60	1.19
38.73	576	42	499.06	13.36	540.24	6.21	552.91	4.01	562.51	2.34
38.78	679	45	590.15	13.08	653.39	3.77	665.59	1.97	671.26	1.14
37.46	798	51	720.68	9.69	796.30	0.21	808.99	1.38	814.15	2.02
37.46	818	50	734.01	10.27	793.57	2.99	806.72	1.38	812.29	0.70
37.30	927	53	817.91	11.77	913.74	1.43	925.72	0.14	933.74	0.73
35.76	1001	50	958.09	4.29	1002.07	0.11	1011.29	1.03	1017.71	1.67
Mean E (%)			**-**	**12.25**	**-**	**3.55**	**-**	**1.82**	**-**	**1.56**

Given that the MAPE obtained for the (256×64×64) dimension is very close to that of the GNLM (1.56% compared to 1.47%), no additional dimensions were evaluated. This value can be interpreted as a plateau, representing the model's intrinsic error, a threshold below which error reduction becomes negligible compared to the additional computational cost.

To complement the analysis, Figure 5 presents the evaluation of the irradiance estimation error as a function of the PV module voltage under four distinct irradiance and temperature conditions. Each subplot illustrates the estimation performance of the different LUT dimensions across the module's entire operational voltage range.

The (256×64×64) configuration yielded the lowest MAPE under MPP conditions, which are the most relevant from an energy generation standpoint. Furthermore, the analysis of estimation errors under different environmental conditions revealed that, in general, larger table dimensions lead to smaller estimation errors across various voltage levels. Therefore, the (256×64×64) configuration was selected as the most suitable LUT size for the proposed system.

3.2. Experimental Results

This stage involved the experimental validation of the proposed system. The behavior of the Canadian Solar CS6W-555MS PV module was emulated using a Regatron laboratory power supply, to which the prototype was connected. This setup allowed for the evaluation of the system's accuracy under both uniform (unshaded) and partial shading conditions. Furthermore, the validation process assessed the performance and reliability of the entire data acquisition and IoT communication, encompassing the microcontroller, the MQTT broker, and the Python script.

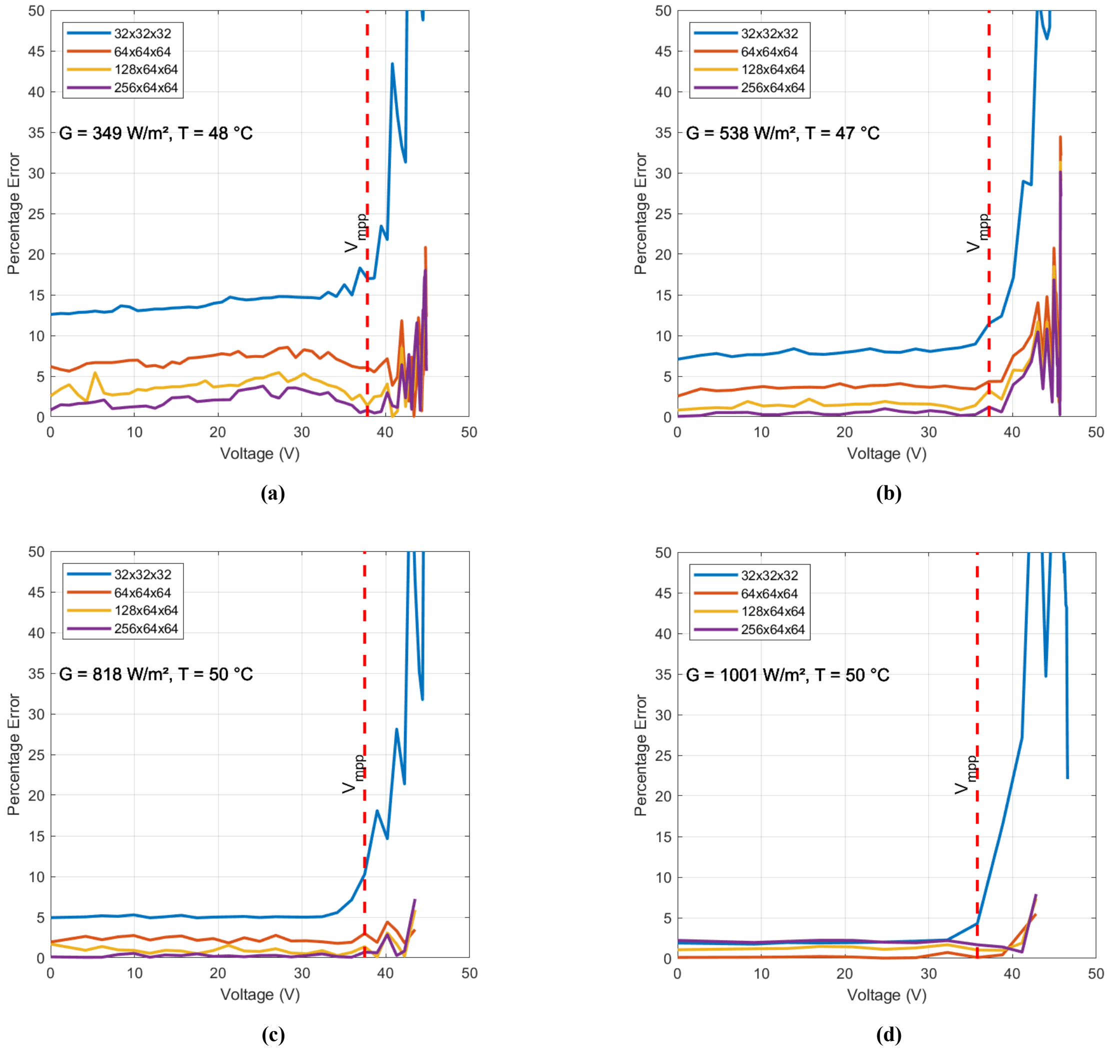

Figure 5: Evaluation of G estimation error as function of PV module voltage for different irradiance and temperature conditions. Results for: (a) G = 349 W/m², T = 48 °C; (b) G = 538 W/m², T = 47 °C; (c) G = 818 W/m², T = 50 °C; and (d) G = 1001 W/m², T = 50 °C.

For the prototype implementation, the MQTT broker was installed on a personal computer, providing a practical setup for system validation. The Python script was configured to run continuously on the same computer, establishing an internal connection with the broker. The microcontroller was connected to the same Wi-Fi network as the computer, enabling communication with the broker through its assigned IP address within the network.

The experimental setup for this validation phase was assembled in a laboratory environment. A programmable Regatron power supply, capable of emulating the behavior of PV modules, was used to simulate the operation of the PV module CS6W-555MS. A resistive load was connected in parallel to the emulated module. The microcontroller prototype was connected to acquire measurements of current, voltage, and temperature (according to Figure 2). Additionally, a secondary DC power supply was required to power the prototype, and a computer was used to monitor the MQTT communication and the irradiance estimation algorithm. Figure 6 presents the assembled experimental configuration.

Once stable communication was established and the experimental setup was properly assembled, tests were conducted under different environmental conditions. For the following experiments, actual I-V curves of the module were used, acquired using the PVA-1000S curve tracer.

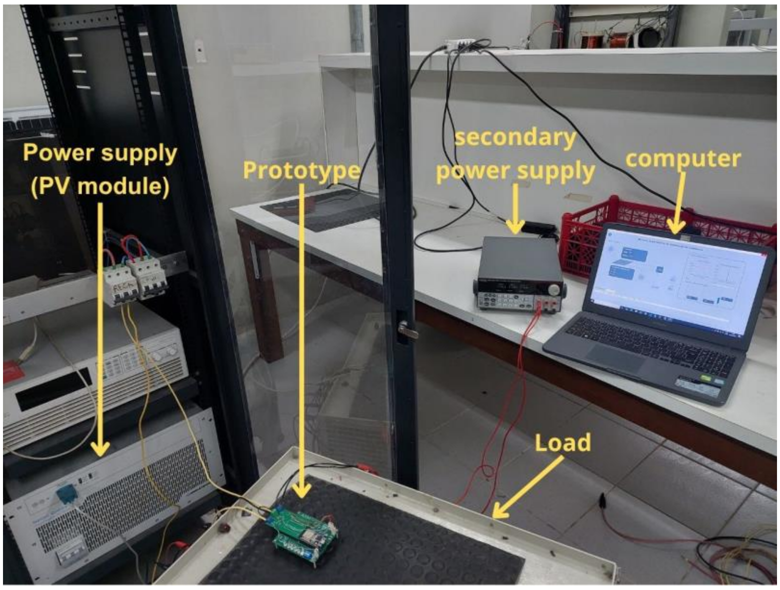

Figure 6: Experimental setup of the irradiance estimator connected to the programmable power supply and to the resistive load.

Initially, the programmable power supply was configured to reproduce ten distinct environmental conditions with uniform irradiance. Since the experiment does not allow for natural module temperature variations, the temperature value was directly input into the estimation algorithm, bypassing the temperature sensor. A constant load resistance of 3 Ω was maintained throughout the experiment. Table 3 presents the considered environmental conditions, the estimation results (Gest), and their corresponding percentage errors.

Table 3: Results of PV module emulation using programmable power supply (Regatron).

G (W/m2)	T (°C)	Gest (W/m2)	Error (%)
280	49	288.3	2.96
349	48	338.6	2.98
405	34	386.6	4.54
479	46	468.1	2.28
538	47	530.6	1.38
641	46	620.2	3.24
709	49	712.3	0.46
785	45	770.1	1.90
798	51	776.1	2.74
818	50	803.7	1.75
Mean (%)		-	2.42

The results obtained for the ten uniform irradiance conditions yielded a MAPE of 2.42%. Although this test is insufficient for a direct comparison with the other estimators mentioned in the introduction, as they were subjected to extensive field operation over several hours, this result successfully demonstrates the correct operation of the proposed algorithm and its fundamental viability for irradiance estimation.

Following the validation under uniform conditions, the system was tested under partial shading scenarios to evaluate its performance in such environments. The programmable power supply was configured to emulate two distinct I-V curves with two steps each. To assess the estimator's behavior across the different characteristic regions of the curve, various load resistance values were applied to control the module's operating point. Figures 7 and 8 present the two emulated I-V curves used in this analysis, highlighting the distinct operating points, the applied load resistances, and the corresponding irradiance estimates obtained at each point.

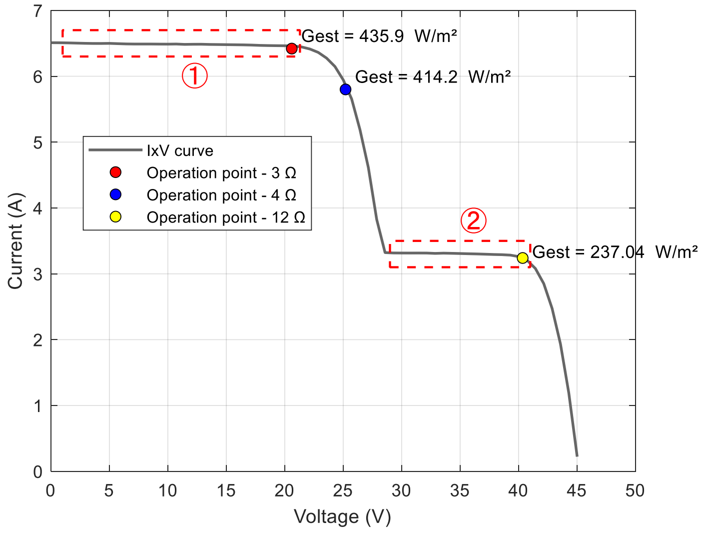

Figure 7: Partial shading scenario for the emulated I–V curve with two irradiance levels (T = 40 °C), showing operating points, load resistances, and estimated irradiance values. Step ①: G = 450 W/m² - irradiance measured by the pyranometer. Step ②: G = 230 W/m² - approximated irradiance value corresponding to the shaded region.

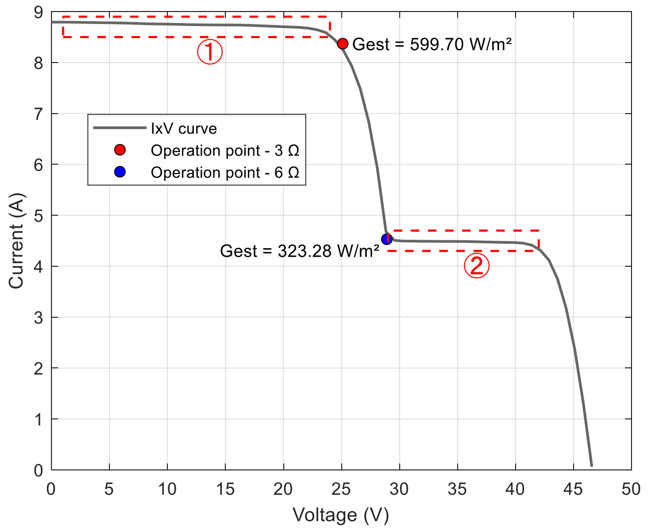

Figure 8: Partial shading scenario for the emulated I–V curve with two irradiance levels (T = 35 °C), showing operating points, load resistances, and estimated irradiance values. Step ①: G = 618 W/m² - irradiance measured by the pyranometer. Step ②: G = 317 W/m² - approximated irradiance value corresponding to the shaded region.

In the first scenario (Figure 7), the operating point at 3 Ω positions the module on the higher irradiance plateau, yielding an estimated irradiance of Gest = 435.9 W/m², with an error of 3.13%. At the 12 Ω operating point, the module operates on the lower irradiance step (approximately G = 230 W/m²), with the estimate falling within the expected range (Gest = 237 W/m²). Since the GNLM applied in the algorithm approximates an I-V curve for uniform irradiance from the (I, V, T) inputs, each operating point is interpreted by the model as a distinct uniform curve rather than as points on the same shaded curve. Consequently, the estimates are coherent with the individual irradiance steps. However, at operating points within the transition region between plateaus, the model yields irradiance values that are intermediate to the step values, as evidenced by the 4 Ω operating point resulting in Gest = 414.2 W/m². This occurs because the model, by design, does not interpret shading effects and will always reconstruct an I-V curve assuming uniform irradiance across the module.

The same underlying principle is observed in the second scenario (Figure 8). At the 3 Ω operating point, corresponding to the higher irradiance level (G = 618 W/m²), the estimate was accurate with Gest = 599.7 W/m², with an error of 2.96%. Conversely, at the 6 Ω operating point, which places the module on the lower irradiance step (approximately G = 317 W/m²), the model correctly estimated the local condition with Gest = 323.3 W/m². These results further confirm the estimator's behavior of interpreting each operating point as belonging to a distinct, uniformly irradiated I-V curve.

4. Conclusions

In this work, an enhanced irradiance estimator was developed and evaluated, featuring robust hardware, high-precision sensing, remote communication, and distributed data processing. The proposed system represents a significant improvement over previous implementations by addressing key limitations in hardware robustness and computational constraints. The decentralization of data processing enabled the use of a LUT that exceeds the microcontroller's storage capacity, allowing for more precise estimations.

The experimental validation confirmed the reliable operation of the IoT communication framework based on MQTT protocol, establishing a solid foundation for remote monitoring applications. Laboratory tests under uniform irradiance conditions demonstrated the system's practical accuracy, with a MAPE of 2.42% across different environmental conditions. Although direct comparison with field-validated estimators requires further testing, these results firmly establish the system's viability for irradiance monitoring applications.

In partial shading scenarios, the estimator provides accurate readings on the higher irradiance steps, which align with pyranometer measurements. On the lower steps, the estimates offer interpretive value by approximating the irradiance level in the shaded areas. However, at operating points within the transition region between steps, the model yields irradiance values intermediate to the actual levels. These results reflect the model's fundamental principle of reconstructing a single, uniform I-V curve from any (I, V, T) point. This behavior underscores a known limitation of the GNLM by Silva et al. (2017), which was not designed for partial shading scenarios. Nevertheless, it does not invalidate the estimator's utility in identifying the different irradiance levels across most operational regions.

The proposed system effectively balances accuracy, cost-effectiveness, and functionality, achieving comparable performance to more complex estimators while maintaining the hardware simplicity essential for widespread PV system integration.

5. References

Alarcon-Maza, K., Herrera-Perez, V., Rodriguez-Flores, J., Pacheco-Cunduri, M., Hernandez-Ambato, J., 2023. Design and experimental validation of an iot data-logger device for indirect measurement of solar irradiance based on a correlation model. *2023 IEEE Green Technologies Conference (GreenTech)*, Denver, 40-45 April.

Barbosa, E.J., Cavalcanti, M.C., Azevedo, G.M.S., Neto, R.C., Barbosa, E.A. O., Bradaschia, F., 2024a. Hybrid GMPPT Technique for Photovoltaic Series Based on Fractional Characteristic Curve. IEEE Journal of Photovoltaics. 14 (1), 170-177.

Barbosa, E.J., Azevedo, G.M.S., Cavalcanti, M.C., Cavalcante, V.M., Bradaschia, F., Limongi, L.R., 2024b. Junction box-integrated irradiance estimator for photovoltaic modules based on IoT technology. IEEE Transactions on Industrial Electronics. 71 (11), 14135-14145.

Carrasco, M., Mancilla-David, F., Ortega, R., 2014. An estimator of solar irradiance in photovoltaic arrays with guaranteed stability properties. IEEE Transactions on Industrial Electronics. 61 (7), 3359-3366.

Chouay, Y., Ouassaid, M., 2024. An accurate real time neural network based irradiance and temperature sensor for photovoltaic applications. Results in Engineering. 21, 101766.

Hajji, M., Yahyaoui, Z., Mansouri, M., Nounou, H., Nounou, M., 2023. Fault detection and diagnosis in grid-connected PV systems under irradiance variations. Energy Reports. 9, 4005-4017.

Lazzaretti, A. E., Costa, C. H., Rodrigues, M. P., Yamada, G. D., Lexinoski, G., Moritz, G. L., Oroski, E., Goes, R. E., Linhares, R. R., Stadzisz, P. C., Omori, J. S., & Santos, R. B., 2020. A Monitoring System for Online Fault Detection and Classification in Photovoltaic Plants. Sensors. 20 (17), 4688.

Lu, H., Zhang, Y., Hao, P., Ma, J., Zhong, H., Gu, T., Yang, M., Zhang, L., 2022. Output performance prediction of PV modules based on power-law model from manufacturer datasheet. Journal of Renewable and Sustainable Energy. 14, 033501.

Madureira, V.S., Chagas, T.P., Jesus, G.Q., 2020. Solar irradiance estimation using Kalman filter. Journal of Control Automation and Electrical Systems. 31, 1447-1457.

Silva, E. A., Bradaschia, F., Cavalcanti, M. C., Nascimento, A. J., Michels, L., Pietta, L. P., 2017. An eight-parameter adaptive model for the single diode equivalent circuit based on the photovoltaic module's physics. IEEE Journal of Photovoltaics. 7 (4), 1115–1123.

Yildiz, T., Gol, M., 2019. A malfunction detection method for PV Systems. *2019 IEEE Milan PowerTech*, Milan, 1-6 June.

Zhang, Y., Hao, P., Lu, H., Gu, T., Yang, M., 2022. A novel method for performance estimation of photovoltaic module without setting reference condition. International Journal of Electrical Power & Energy Systems. 134, 107439.